

Handheld miniature probe integrating diffuse optical tomography with photoacoustic imaging through a MEMS scanning mirror

Hao Yang,¹ Lei Xi,¹ Sean Samuelson,² Huikai Xie,² Lily Yang,³ and Huabei Jiang^{1,*}

¹Department of Biomedical Engineering, University of Florida, Gainesville, FL 32611, USA

²Department of Electrical and Computer Engineering, University of Florida, Gainesville, FL 32611, USA

³Department of Surgery, Emory University, Atlanta, GA 30322, USA

*hjiang@bme.ufl.edu

Abstract: We describe a novel dual-modality imaging approach that integrates diffuse optical tomography (DOT) and photoacoustic imaging (PAI) through a miniaturized handheld probe based on microelectromechanical systems (MEMS) scanning mirror. We validate this dual-modal DOT/PAI approach using extensive phantom experiments, and demonstrate its application for tumor imaging using tumor-bearing mice systematically injected with targeted contrast agents.

©2013 Optical Society of America

OCIS codes: (110.6960) Tomography; (170.0110) Imaging systems; (170.5120) Photoacoustic imaging.

References and links

1. H. Jiang, *Diffuse Optical Tomography: Principles and Applications* (CRC Press, 2010).
2. L. V. Wang, "Multiscale photoacoustic microscopy and computed tomography," *Nat. Photonics* **3**(9), 503–509 (2009).
3. H. Jiang, N. V. Iftimia, Y. Xu, J. A. Eggert, L. L. Fajardo, and K. L. Klove, "Near-infrared optical imaging of the breast with model-based reconstruction," *Acad. Radiol.* **9**(2), 186–194 (2002).
4. B. J. Tromberg, B. W. Pogue, K. D. Paulsen, A. G. Yodanis, D. A. Boas, and A. E. Cerussi, "Assessing the future of diffuse optical imaging technologies for breast cancer management," *Med. Phys.* **35**(6), 2443–2451 (2008).
5. Z. Yuan, Q. Zhang, E. Sobel, and H. Jiang, "Three-dimensional diffuse optical tomography of osteoarthritis: initial results in the finger joints," *J. Biomed. Opt.* **12**(3), 034001 (2007).
6. Z. Yuan, Q. Zhang, E. S. Sobel, and H. Jiang, "Tomographic x-ray-guided three-dimensional diffuse optical tomography of osteoarthritis in the finger joints," *J. Biomed. Opt.* **13**(4), 044006 (2008).
7. J. C. Hebden, "Advances in optical imaging of the newborn infant brain," *Psychophysiology* **40**(4), 501–510 (2003).
8. D. A. Boas, A. M. Dale, and M. A. Franceschini, "Diffuse optical imaging of brain activation: approaches to optimizing image sensitivity, resolution, and accuracy," *Neuroimage* **23**(1 Suppl 1), S275–S288 (2004).
9. C. Li, H. Zhao, B. Anderson, and H. Jiang, "Multispectral breast imaging using a ten-wavelength, 64 x 64 source/detector channels silicon photodiode-based diffuse optical tomography system," *Med. Phys.* **33**(3), 627–636 (2006).
10. H. Jiang, K. D. Paulsen, U. L. Osterberg, and M. S. Patterson, "Frequency-domain near-infrared photo diffusion imaging: initial evaluation in multitarget tissuelike phantoms," *Med. Phys.* **25**(2), 183–193 (1998).
11. Q. Zhang, Z. Liu, P. R. Carney, Z. Yuan, H. Chen, S. N. Roper, and H. Jiang, "Non-invasive imaging of epileptic seizures in vivo using photoacoustic tomography," *Phys. Med. Biol.* **53**(7), 1921–1931 (2008).
12. L. Yin, Q. Wang, Q. Zhang, and H. Jiang, "Tomographic imaging of absolute optical absorption coefficient in turbid media using combined photoacoustic and diffusing light measurements," *Opt. Lett.* **32**(17), 2556–2558 (2007).
13. X. Li, L. Xi, R. Jiang, L. Yao, and H. Jiang, "Integrated diffuse optical tomography and photoacoustic tomography: phantom validations," *Biomed. Opt. Express* **2**(8), 2348–2353 (2011).
14. A. Q. Bauer, R. E. Nothdurft, T. N. Erpelding, L. V. Wang, and J. P. Culver, "Quantitative photoacoustic imaging: correcting for heterogeneous light fluence distributions using diffuse optical tomography," *J. Biomed. Opt.* **16**(9), 096016 (2011).
15. C. Xu, P. D. Kumavor, A. Aguirre, and Q. Zhu, "Investigation of a diffuse optical tomography-assisted quantitative photoacoustic tomography in reflection geometry," *Proc. SPIE* **7899**, 78990U (2011).
16. W. Jung, D. T. McCormick, Y. C. Ahn, A. Sepehr, M. Brenner, B. Wong, N. C. Tien, and Z. Chen, "In vivo three-dimensional spectral domain endoscopic optical coherence tomography using a microelectromechanical system mirror," *Opt. Lett.* **32**(22), 3239–3241 (2007).

17. W. Piyawattanametha and T. D. Wang, "MEMS-based dual axes confocal microendoscopy," *IEEE J. Sel. Top. Quantum Electron.* **16**(4), 804–814 (2010).
18. L. Xi, J. Sun, Y. Zhu, L. Wu, H. Xie, and H. Jiang, "Photoacoustic imaging based on MEMS mirror scanning," *Biomed. Opt. Express* **1**(5), 1278–1283 (2010).
19. L. Xi, S. R. Grobmyer, L. Wu, R. Chen, G. Zhou, L. G. Gutwein, J. Sun, W. Liao, Q. Zhou, H. Xie, and H. Jiang, "Evaluation of breast tumor margins in vivo with intraoperative photoacoustic imaging," *Opt. Express* **20**(8), 8726–8731 (2012).
20. C. Li and H. Jiang, "A calibration method in diffuse optical tomography," *J. Opt. A, Pure Appl. Opt.* **6**(9), 844–852 (2004).
21. H. Jiang, Y. Xu, and N. Ifimia, "Experimental three-dimensional optical image reconstruction of heterogeneous turbid media from continuous-wave data," *Opt. Express* **7**(5), 204–209 (2000).
22. H. Jiang, K. D. Paulsen, U. L. Osterberg, and M. S. Patterson, "Improved continuous light diffusion imaging in single- and multi-target tissue-like phantoms," *Phys. Med. Biol.* **43**(3), 675–693 (1998).
23. C. Wu, X. Liang, and H. Jiang, "Metal nanoshells as a contrast agent in near-infrared diffuse optical tomography," *Opt. Commun.* **253**(1-3), 214–221 (2005).
24. L. Yang, X. H. Peng, Y. A. Wang, X. Wang, Z. Cao, C. Ni, P. Karna, X. Zhang, W. C. Wood, X. Gao, S. Nie, and H. Mao, "Receptor-targeted nanoparticles for in vivo imaging of breast cancer," *Clin. Cancer Res.* **15**(14), 4722–4732 (2009).

1. Introduction

Diffuse optical tomography (DOT) is an emerging modality capable of offering high contrast in both tissue absorption and scattering with centimeter penetration [1], while photoacoustic imaging (PAI) is a rapidly growing technique that can provide high resolution imaging of tissue absorption with millimeter penetration [2]. DOT has been so far applied to the detection of breast cancer, arthritis and functional brain activities [3–11], and PAI has been focused mostly on imaging vasculatures with limited application in tumor detection [2].

Combining DOT and photoacoustic imaging into a single platform is a natural and valuable approach since such combination can take the advantages of both modalities. We reported for the first time such approach in 2007 [12] and have seen now several other studies in this regard [13–15]. These prior studies mostly were focused on a realization of combined DOT and photoacoustic imaging for large tissue imaging such as breast cancer detection. The goal of the current work is to realize a combination of DOT with PAI for relatively small tissue imaging (less than 1cm depth). An example of small tissue imaging is image-guided surgery. In such case, DOT will be used to estimate the location/size of the deeply located tumors and PAI will then be used to precisely identify the tumor margins when the imaging probe is close to the tumors.

We achieve the integration of DOT and PAI through a miniaturized handheld probe based on microelectromechanical systems (MEMS). MEMS is a powerful technology for device miniaturization and has been applied to optical coherent tomography and confocal microscopy [16,17]. We have recently demonstrated its application in photoacoustic imaging [18,19]. Here we describe its application as a central component for the integration of DOT and PAI. We present three-dimensional DOT and PAI images using our DOT/PAI from a series of phantom and tumor-bearing mouse experiments.

2. Materials and methods

The schematic of the MEMS-based DOT/PAI system is shown in Fig. 1(a), in which a MEMS mirror [Fig. 1(b)], embedded in a small-diameter imaging probe (Fig. 1(a) (left) and Fig. 1(c)), is used to perform laser beam scanning and an array of optic fibers coupled with a PZT ring-shaped transducer (5.5MHz central frequency) [Fig. 1(c)], attached to the end of the imaging probe, are used to detect the diffused light and acoustic signal, respectively. The ultrasound transducer is placed 1cm inside the probe to keep a distance from the surface of object. The home-made MEMS mirror (aperture size: $1 \times 1 \text{ mm}^2$ and footprint size: $2 \times 2 \text{ mm}^2$) has four electrothermal bimorph-based actuators made from a lateral-shift-free large-vertical-displacement (LSF-LVD) design [18,19]. 2D scanning can be realized by applying different voltages to the four actuators.

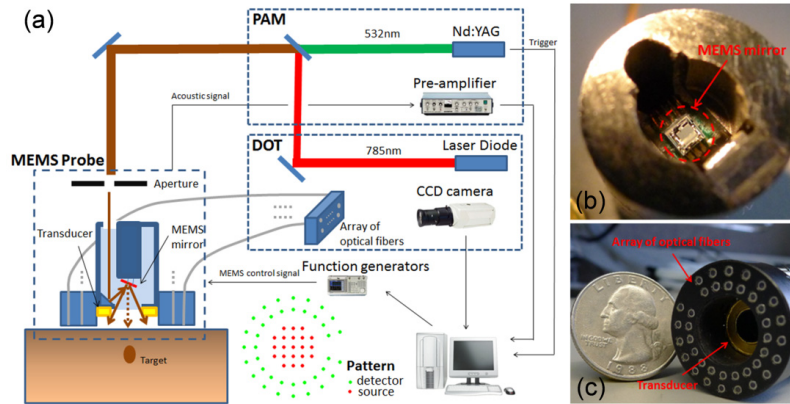


Fig. 1. (a) Schematic of the PAI/DOT imaging system. Photograph of the MEMS mirror (b) and the integrated optic fibers and ultrasound transducer probe (c).

The PAI subsystem was previously described in detail in [18,19]. Briefly, a light beam of 0.8mm in diameter from a pulsed Nd:YAG 532 nm laser (532nm, 20ns pulse width, 10Hz repetition rate; EKSPALA, NL 303HT, Lithuania) is delivered via the imaging probe to the surface of the object and the ring-shaped transducer detects the laser-induced photoacoustic signal. By MEMS scanning the laser beam, a 2D PAI image covering a field of $6\text{mm} \times 6\text{mm}$ is obtained. The image formation method is similar to that for B-mode ultrasound imaging [2]. In the experiments, the transducer and the sample are immersed in water to minimize ultrasound attenuation. The axial resolution of the PAI subsystem is less than 0.5mm and the lateral resolution is 0.2-0.7mm depending on the target depth [18,19].

In the DOT subsystem, the laser beam generated by a continuous-wave (CW) 780nm diode laser (Openxt, HL7301MG, Japan), is scanned on the surface of the object via the MEMS mirror. Two function generators (Tektronix, Afg3022B, OR) connected with the MEMS mirror are used to direct the scanning position of the laser beam precisely. As shown in Fig. 1(c), the optical fiber array (25mm in diameter) contains 38 optical fiber bundles (1.2mm in diameter each). The pattern of the source (red) and detector (green) positions is shown in Fig. 1. There are totally 21 scanned source positions and the distance between two nearby sources is 2mm. Thirty-eight detector fiber bundles are arranged along two circular paths having 16 mm and 21 mm in diameter, respectively. Diffused light collected by the detector fiber array is recorded by a 1024×1024 pixels CCD camera (Princeton instruments, PIXIS, NJ). The DOT images are reconstructed using our finite element based algorithms and the spatial resolution is about 3-4mm [1].

In our PAI/DOT system, a Visual C++ program is used to control the function generators, CCD camera, and the data acquisition process. The data acquisition time lengths are about 5 minutes for PAI and 1 minute for DOT, respectively.

3. Results and discussion

To demonstrate the ability of this integrated DOT/PAI probe, several sets of phantom experiments were performed. In the phantom preparation, tissue absorption and scattering were simulated with India ink and Intralipid, respectively. Agar powder (2%) was used to solidify the mixed Intralipid-India ink solution. The background of the phantom in this paper had an absorption coefficient of $\mu_a = 0.01 \text{ mm}^{-1}$ and a reduced scattering coefficient of $\mu'_s = 0.6 \text{ mm}^{-1}$. In the DOT reconstructions, a single mesh of 1560 nodes and 7056 triangular elements was applied, and the images were converged within 15 iterations in a 3.2GHz PC with 4-GB memory, taking about 60s. A calibration method based on a homogeneous phantom was used to eliminate the system errors [20-23].

To evaluate this integrated probe in terms of target depth, and contrast and size sensitivity, a series of phantom experiments were conducted, in which common phantoms/objects were used for both DOT and PAI.

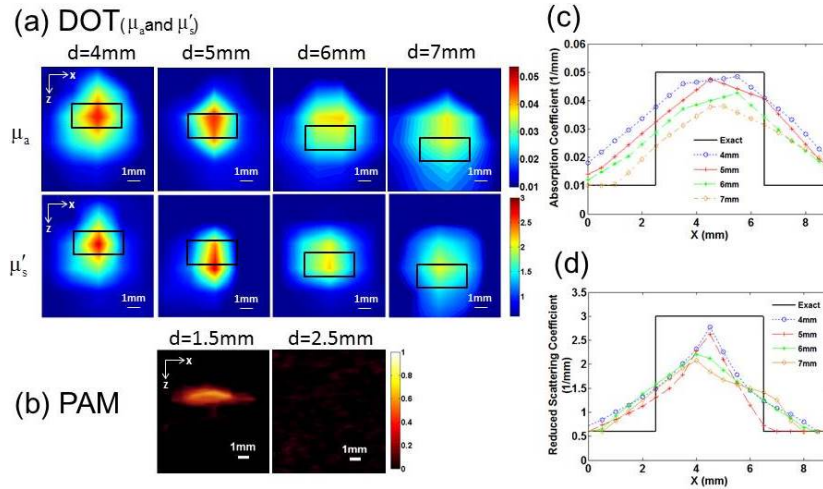


Fig. 2. (a) Reconstructed μ_a and μ'_s images from DOT when the target was located at a depth of 4, 5, 6 and 7mm, respectively, in which d is the target depth and the small black box indicates the exact target location. (b) Recovered PAI images when the target was located at a depth of 1.5 and 2.5mm, respectively. The contrast in both the absorption and scattering coefficients was 5:1 for all the cases. Recovered μ_a (c) and μ'_s (d) values along a transect crossing the center of each target ($z = 6, 5, 4$ and 3mm , respectively) for the images shown in Fig. 2(a).

Figure 2 shows the reconstructed absorption coefficient and reduced scattering coefficient images by DOT (a) and PAI images (b) of a small cylindrical target (4mm in diameter and 2mm in height) embedded at different depths. To analyze the images quantitatively, we plotted the optical property profiles (μ_a (Fig. 2(c)) and μ'_s (Fig. 2(d))) along a transect crossing each of the four targets ($z = 6\text{mm}$, 5mm , 4mm and 3mm , respectively). For the cases of 4mm and 5mm depths, both μ_a and μ'_s are close to the actual value (0.05 mm^{-1}). However, the accuracy of μ_a and μ'_s recovery for the cases of 6mm and 7mm depths is decreased relative to the cases of 4mm and 5mm depths. It is also noted from Figs. 2(a) and 2(b) that the recovered value of μ_a is more accurate than μ'_s . From Fig. 2, we can see that the target was well reconstructed at a depth of up to 7mm for DOT, while we note that the target size was overestimated and the location shift little due to strong light scattering. Whereas we see that the target was detectable at a depth of up to 1.5mm with clearly higher resolution for PAI. It is also noticed that target could not be identified in the PAI images at depths beyond 2.5mm for PAI.

Figure 3 presents the recovered μ_a and μ'_s images by DOT (a) and PAI images (b) when a single target with a diameter of 4mm, 2mm, 1mm and 0.5mm was embedded 1.5mm below the surface of the phantom. We can observe that only the 4mm-diameter target can be reconstructed by DOT, while all the targets can be well recovered by PAI. In Fig. 3(c), we plotted the normalized photoacoustic signal amplitude along a transect crossing the center of each target shown in Fig. 3(b). The Full Width at Half Maximum (FWHM) of the normalized amplitude matches very well with the exact size of the target, demonstrating the high spatial resolution of PAI.

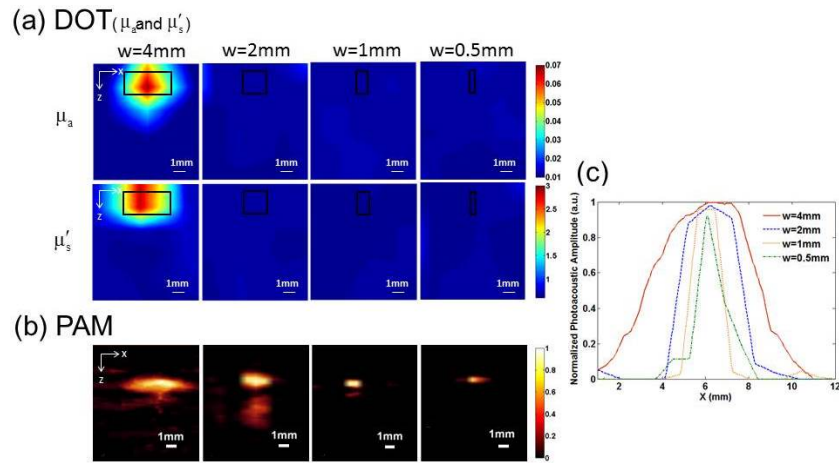


Fig. 3. Reconstructed μ_a and μ'_s images from DOT (a) and PAI (b) images for a target having 4, 2, 1 and 0.5mm in diameter, respectively, in which w is the diameter of the target and the black box indicates the exact target location. The contrast in both the absorption and scattering coefficients was 7:1. (c) Normalized photoacoustic signal amplitude along a transect crossing the center of each target for the images shown in (b).

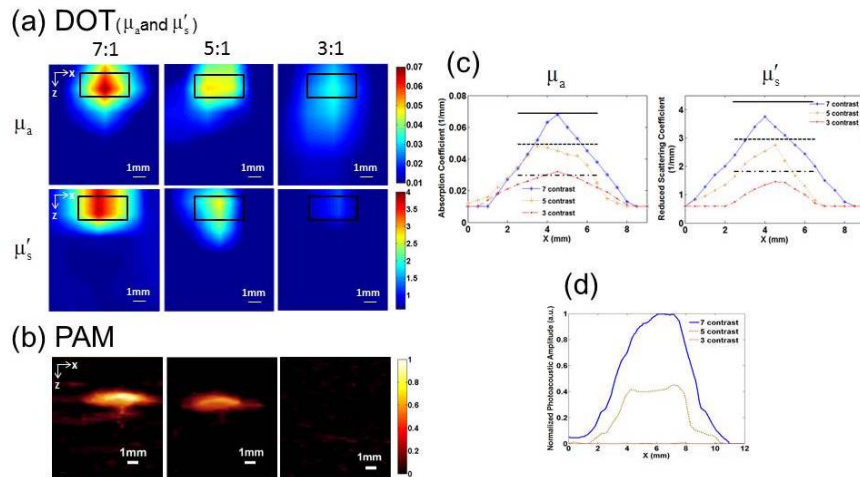


Fig. 4. Reconstructed μ_a and μ'_s images from DOT (a) and PAI (b) images for a target having 7, 5 and 3 times contrast, respectively. The target had a 4mm diameter and 2mm thickness. The back box in (a) indicates the exact target location. (c) Recovered μ_a (left) and μ'_s (right) values along a transect crossing the center of each target for the images shown in (a). (d) Normalized photoacoustic signal amplitude along a transect crossing the center of each target for the images shown in (b).

Figure 4 gives the DOT (μ_a and μ'_s) (a) and PAI (b) images for a target having 7, 5, and 3 times contrast for both the μ_a and μ'_s embedded in the phantom at a depth of 1.5mm. We note that the target can be well recovered by DOT for all the cases, while the target with high contrast can be recovered and the low contrast target cannot be detected by PAI. In Fig. 4(c), we plotted the recovered μ_a and μ'_s values along a transect crossing each of the three targets ($z = 8.5\text{mm}$) for the images shown in Fig. 4(a). The recovered μ_a for all the three cases are close to the exact value, while μ'_s values are slightly lower than the exact values. We also

plotted the normalized photoacoustic signal amplitude along a transect crossing the center of each target shown in Fig. 4(b). Again, the FWHM agrees well with the exact target size.

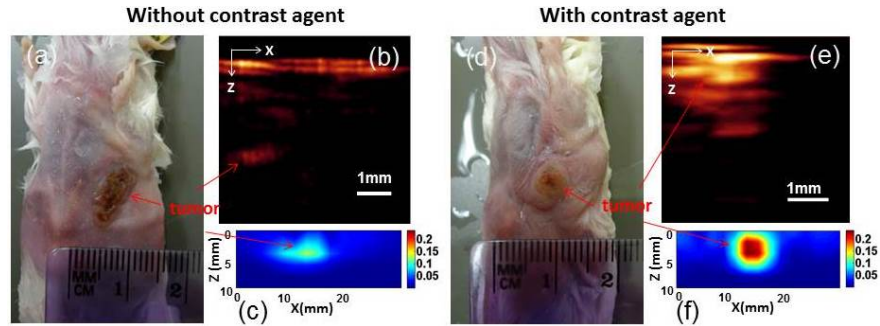


Fig. 5. (a) Photograph of the tumor-bearing mouse without (a) and with contrast agent (100pmole NIR-830-ATF-IONP) (d). A sagittal slice of PAI (b and e) and DOT (μ_a) (c and f).

To demonstrate the in vivo imaging ability of our DOT/PAI probe, tumor-bearing mice without and with the use of targeted contrast agent were imaged. Figure 5 shows the recovered PAI (b) and DOT (c) images for a control tumor-bearing mouse without contrast agent administrated, while Figs. 5(d)-5(f) present the PAI (e) and DOT (f) images for a tumor-bearing mouse systematically injected with 100pmole NIR-830-mATF-IONP, a peptide conjugated molecular probe loaded with both near-infrared dye and iron oxide nanoparticles that can target tumor cell receptors [24]. For the control case, we see that both PAI and DOT detected the tumor with low contrast (Figs. 5(b) and 5(c)). When NIR-830-mATF-IONP was administrated, dramatically improved detection of tumor for PAI and clearly enhanced contrast (tumor-to-tissue) for DOT are obtained (Figs. 5(e) and 5(f)). The artifact seen at the top of the images is due to the strong absorption of blood block existing at the mouse skin. The results clearly show the advantages of this dual modal probe: The tumor margins can be identified by PAI due to its high spatial resolution; meanwhile, the quantitative information of optical properties of tumor can be provided by DOT.

The primary advantage of the combined miniature DOT/PAI probe presented here is its potential for endoscopic imaging. While promising, we are aware of its limitations, such as the long data acquisition time, not-optimized probe size, etc.. We plan to use a laser with 1 kHz repetition rate, making real-time imaging possible. Moreover, we will improve the spatial resolution of PAI by using a transducer with higher central frequency and focal light beam. We will also further miniaturize the probe size with optimized optical/acoustic alignment.

4. Conclusions

We have presented a novel MEMS-based DOT/PAI imaging system and evaluated it with both phantom and animal experiments. It has been demonstrated that this MEMS scanning mirror based miniaturized probe offers a great potential to develop a compact handheld probe for future clinical applications. To our best knowledge, this is the first report of a miniaturized DOT/PAI handheld probe based on a MEMS scanning mirror, which integrates the advantages of two different imaging methods. We plan to apply an improved miniature probe for endoscopic imaging of GI tracks.

Acknowledgment

This research was supported in part by a grant from the National Institutes of Health (R21 CA161384).